

Pauli blockade microscopy of quantum dots

E. Wach and B. Szafran

AGH University of Science and Technology,
Faculty of Physics and Applied Computer Science,
al. Mickiewicza 30, 30-059 Kraków, Poland

We propose a spin-sensitive scanning probe microscopy experiment on double quantum dots in Pauli blockade conditions. Electric spin resonance is induced by an AC voltage applied to the scanning gate which induces lifting of the Pauli blockade of the current. The stationary Hamiltonian eigenstates are used as a basis for description of the spin dynamics with the AC potential of the probe. For the two-electron system we evaluate the transitions rates from triplet T_+ state to singlet S or triplet T_0 states, i.e. to conditions in which the Pauli blockade of the current is lifted. The rates of the spin-flip transitions are consistent with the transition matrix elements and strongly dependent on the tip position. Probing the spin densities and identification of the final transition state are discussed.

I. INTRODUCTION

The potential landscape within the electron gas buried shallow beneath the surface of semiconductor¹⁻⁹, quantum wires^{10,11}, carbon nanotubes¹²⁻¹⁴, graphene¹⁵⁻¹⁷ can be modified in a controllable manner by potential of an external gate. This fact was used for development of a scanning gate microscopy technique^{18,19}, in which the current or conductance maps are taken as a function of the position of a charged tip of an atomic force microscope floating above the surface of the system^{18,19}. The technique produces spatial information on the charge transport in open systems, including quantum point contacts^{1,2,6,7}, or quantum rings¹⁸, magnetic focusing^{5,16,17}, etc. The method was also used to probe the states localized in quantum dots^{3,4,8,10-12,14,15}, where the potential of the tip switches on or off the Coulomb blockade²⁰ of the current flow. The technique was nicknamed a Coulomb blockade microscopy²¹⁻²⁴.

In the present paper we propose to use the external gate of the atomic force microscope on the system in which the flow of the current is blocked by the Pauli exclusion principle. The most elementary system in which the Pauli blockade²⁵⁻³¹ is the double quantum dot biased in a manner that each of the dots stores a single electron and the electrons possess identical spins [see Fig. 1(a)]. The electron hopping from one dot to the other can occur only provided that the spin of one of the electrons is flipped. The spin-flip can be intentionally induced by electron spin resonance using microwave radiation³¹ or, in spin-orbit coupled systems, by electric-dipole spin resonance driven by the AC voltage applied to one of the gates^{27-30,32,33}. The idea investigated in this paper is to use the scanning probe as the gate which provides the AC perturbation [see Fig. 1] that drives the spin polarized triplet T_+ to systems in which the Pauli blockade is lifted: the singlet S or T_0 , which in III-V materials are mixed by the hyperfine field³⁴. The maps of the transition rates bear signatures of the single-electron wave functions or the convolution of the majority and minority spin components with the potential of the tip. We demonstrate that it is possible to perform imaging of the

spatial distribution of the spin in a confined spin-orbit coupled system and to identify the final state S or T_0 of the spin-transition lifting the Pauli blockade by the form of the map.

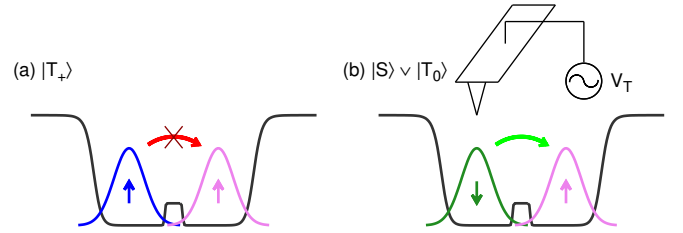


FIG. 1. Schematic drawing of the system: the confining potential $V_c(x, 0)$ of a double quantum dot, each dot stores a single electron. (a) The system is prepared in the spin-polarized triplet state $|T_+\rangle$. Both spins are identical (up), the electron hopping is forbidden. (b) The AC voltage is applied to the AFM tip and causes the spin-flip; the Pauli blockade is lifted.

II. THEORY

A. Solution of the time-independent Schrödinger equation

We investigate a single electron confined in a rectangular quantum dot and an electron pair in two tunnel-coupled quantum dots assuming a strictly two-dimensional model of confinement. The one-electron Hamiltonian

$$h = \left(\frac{(-i\hbar\nabla + e\mathbf{A})^2}{2m^*} + V_c(\mathbf{r}) \right) \mathbf{1} + H_{SO} + \frac{1}{2}g^*\mu_B B\sigma_z \quad (1)$$

is taken in the effective-mass-approximation form, where m^* and g^* stand for the effective mass and Landé factor, respectively, $\mathbf{1}$ is the identity matrix, $V_c(\mathbf{r})$ is the confinement potential, and H_{SO} introduces Dresselhaus spin-orbit interaction³⁵. The last term describes the spin

Zeeman effect in the presence of a static magnetic field B oriented perpendicular to the plane of confinement. The symmetric gauge $\mathbf{A} = B(-\frac{y}{2}, \frac{x}{2}, 0)$ is used.

We account for the linear Dresselhaus SO term

$$H_{\text{SO}} = \gamma \langle k_z^2 \rangle [\sigma_x k_x - \sigma_y k_y]. \quad (2)$$

The cubic component of the Dresselhaus term produces small effects as compared to the linear one and thus is neglected³⁶. $\sigma_x, \sigma_y, \sigma_z$ are Pauli matrices and k_x, k_y, k_z are the components of the wave vector \mathbf{k} , while $\hbar\mathbf{k} = \mathbf{p} = -i\hbar\nabla + e\mathbf{A}$. The linear Dresselhaus constant $\gamma \langle k_z^2 \rangle$ for two-dimensional Hamiltonian is obtained by

$$\gamma \langle k_z^2 \rangle = \gamma \frac{\pi^2}{d^2}, \quad (3)$$

where γ is the Dresselhaus bulk SO coupling constant and d means the height of the QD ($d = 5.42$ nm is taken). We use $\gamma = 32.2$ meVnm³ assuming the QD is made of In_{0.5}Ga_{0.5}As alloy³⁷, for which $\gamma \langle k_z^2 \rangle \approx 10.82$ meVnm. The other parameters are calculated as arithmetic average of GaAs and InAs values, i.e. $m^* = 0.0465m_0$, $g^* = -8.97$ ^{38,39} and dielectric constant $\epsilon = 13.5$ ⁴⁰. We assume that the 2DEG is symmetrically doped. The potentials inducing the lateral confinement in quantum dots are shallow and the corresponding electric fields are weak which allows us to neglect the Rashba spin-orbit interaction.

In the following we consider confinement potential of the profile

$$V_c(\mathbf{r}) = -\frac{V_0}{\left(1 + \left[\frac{x^2}{R_x^2}\right]^{10}\right) \left(1 + \left[\frac{y^2}{R_y^2}\right]^{10}\right)} + \frac{V_b}{\left(1 + \left[\frac{x^2}{R_b^2}\right]^{10}\right) \left(1 + \left[\frac{y^2}{R_y^2}\right]^{10}\right)}, \quad (4)$$

with the depth of the quantum dot/dots $V_0 = 50$ meV and a flat bottom of nearly rectangular shape with dimensions $2R_x \times 2R_y$ ($R_x = 45$ nm, $R_y = 20$ nm). $R_b = 5$ nm defines the interdot barrier thickness ($2R_b$) and V_b is the barrier height. In the case of a single quantum dot $V_b = 0$. For two tunnel-coupled quantum dots we assume $V_b = 10$ meV. The confining potential and the ground-state charge density for both the single and the double quantum dot are shown in Fig. 2.

We solve the one-electron eigenequation by diagonalization using the basis of multicenter Gaussian functions $f_p(\mathbf{r})$:

$$f_p(\mathbf{r}) = \frac{1}{\alpha_G \sqrt{\pi}} \exp \left[-\frac{(\mathbf{r} - \mathbf{R}_p)^2}{2\alpha_G^2} + \frac{ieB}{2\hbar} (xY_p - yX_p) \right]. \quad (5)$$

The centers of Gaussians $\mathbf{R}_p = (X_p, Y_p)$ are distributed on a rectangular mesh of $M \times N$ points. We use 25×11 basis functions. The n -th eigenfunction is expanded as

$$\psi_n(\mathbf{r}, s) = \sum_p \sum_{s \in \{\uparrow, \downarrow\}} a_{p,s}^{(n)} \chi_s f_p(\mathbf{r}), \quad (6)$$

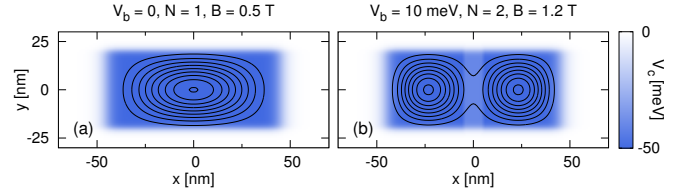


FIG. 2. The contours of the charge density for (a) a single electron ($N = 1$) confined in the single rectangular elongated quantum dot at $B = 0.5$ T; (b) two electrons ($N = 2$) in two tunnel-coupled quantum dots at $B = 1.2$ T. The shades of blue show the confining potential $V_c(x, y)$.

where χ_s are the eigenstates of σ_z matrix. The parameter α_G and the distance between the centers \mathbf{R}_p are optimized variationally.

The eigenequation of two-electron Hamiltonian

$$H = h_1 + h_2 + \frac{e^2}{4\pi\epsilon_0 |\mathbf{r}_1 - \mathbf{r}_2|} \quad (7)$$

is solved by the configuration-interaction method. Two-electron wave functions are expressed by the linear combinations of the Slater determinants formed from the spin-orbitals $\psi_k(\mathbf{r}, s)$:

$$\Psi_n(\mathbf{r}_1, \mathbf{r}_2, s_1, s_2) = \frac{1}{\sqrt{2}} \sum_k b_k^{(n)} [\psi_{k_1}(\mathbf{r}_1, s_1) \psi_{k_2}(\mathbf{r}_2, s_2) - \psi_{k_2}(\mathbf{r}_1, s_1) \psi_{k_1}(\mathbf{r}_2, s_2)]. \quad (8)$$

We take 30 single-electron spin-orbitals which give convergence of the energies with a precision better than $0.1 \mu\text{eV}$ and produce $\binom{30}{2} = 435$ Slater determinants.

We assume the effective tip potential is short-range⁴¹ and use the Lorentzian formula

$$V_T(\mathbf{r}; \mathbf{r}_{\text{tip}}) = \frac{V_{\text{tip}}}{\left(\frac{x-x_{\text{tip}}}{d_{\text{tip}}}\right)^2 + \left(\frac{y-y_{\text{tip}}}{d_{\text{tip}}}\right)^2 + 1}, \quad (9)$$

where $V_{\text{tip}} = 5$ meV is the height of the potential maximum induced by the tip placed at position $\mathbf{r}_{\text{tip}} = (x_{\text{tip}}, y_{\text{tip}})$ above the confinement plane. $d_{\text{tip}} = 20$ nm defines the width of the Lorentzian. The time dependence is introduced to Hamiltonian by the periodic modulation of the tip potential:

$$h'(t) = h + V_T(\mathbf{r}; \mathbf{r}_{\text{tip}}) \sin(\omega t) \quad (10)$$

for the one-electron Hamiltonian, and

$$H'(t) = H + [V_T(\mathbf{r}_1; \mathbf{r}_{\text{tip}}) + V_T(\mathbf{r}_2; \mathbf{r}_{\text{tip}})] \sin(\omega t) \quad (11)$$

for the two-electron case.

For the single electron the system is prepared in an initial state $\psi_i(\mathbf{r}, s) = \psi_0(\mathbf{r}, s) \equiv \psi(\mathbf{r}, s, t = 0)$. The expansion in the basis given by the eigenstates $\psi_n(\mathbf{r}, s)$

$$\psi(\mathbf{r}, s, t) = \sum_n c_n(t) \psi_n(\mathbf{r}, s) \exp\left(-\frac{iE_n t}{\hbar}\right) \quad (12)$$

describes time evolution of the wave function. By inserting the expansion (12) to the time-dependent Schrödinger equation

$$i\hbar \frac{\partial \psi(\mathbf{r}, s, t)}{\partial t} = h'(t)\psi(\mathbf{r}, s, t) \quad (13)$$

one can obtain a system of differential equations

$$\frac{dc_k(t)}{dt} = -\frac{i}{\hbar} \sum_n c_n(t) \sin(\omega t) \cdot \langle \psi_k | V_T(\mathbf{r}; \mathbf{r}_{\text{tip}}) | \psi_n \rangle \exp(-i\omega_{nk}t), \quad (14)$$

where $\omega_{nk} = \frac{E_n - E_k}{\hbar}$. The equations are solved for the expansion coefficients $c_k(t)$ using finite-difference methods: iterative Crank-Nicolson scheme and the Askar-Cakmak method⁴².

Finally, the probability of effecting a transition from state $\psi_i(\mathbf{r}, s)$ to state $\psi_k(\mathbf{r}, s)$ after time t is given by

$$P_{i \rightarrow k}(t) = |\langle \psi_k | \psi(t) \rangle|^2 = |c_k(t)|^2. \quad (15)$$

The two-electron time-dependent Schrödinger equation for $\Psi(\mathbf{r}_1, \mathbf{r}_2, s_1, s_2, t)$ is solved in the same way.

B. Time-dependent perturbation theory

The exact solution of Eq. (14) produces the direct (single-photon) and the fractional (multiphoton) resonances for the frequencies $\omega = \omega_{ki}$ and $\omega = \omega_{ki}/m$ ($m \in \{2, 3, \dots\}$), respectively. The direct resonances, that are distinctly wider than the fractional ones, can be explained within the time-dependent perturbation theory of the first order. In the perturbation expansion

$$c_k(t) = c_k^{(0)} + c_k^{(1)}(t) + \dots \quad (16)$$

$c_k^{(0)}$ is independent of time and corresponds to the initial state: $c_k^{(0)} = \delta_{ki}$. The formula for the first-order correction reads as

$$c_k^{(1)}(t) = -\frac{i}{\hbar} \int_0^t \langle \psi_k | V_T | \psi_i \rangle \sin(\omega t') \exp(i\omega_{ki}t') dt'. \quad (17)$$

In particular, for $k \neq i$ the probability $P_{i \rightarrow k}(t)$ in the first-order approximation depends mainly on the matrix elements $\langle \psi_k | V_T | \psi_i \rangle$.

III. RESULTS AND DISCUSSION

This Section is organized in the following way. First we discuss the spin-flipping transition for a single electron in a single quantum dot [Fig. 2(a)]. Then, we proceed to description of spin transitions in the two-electron system for a double quantum dot [Fig. 2(b)].

A. Single electron in elongated quantum dot

The single-electron energy spectrum for the quantum dot of Fig. 2(a) is displayed in Fig. 3. The energy effect of the spin-orbit coupling is small and amounts in a shift of the energy levels for $B = 0$, and opening of the avoided crossings between energy levels that possess opposite spins in the absence of SO coupling.

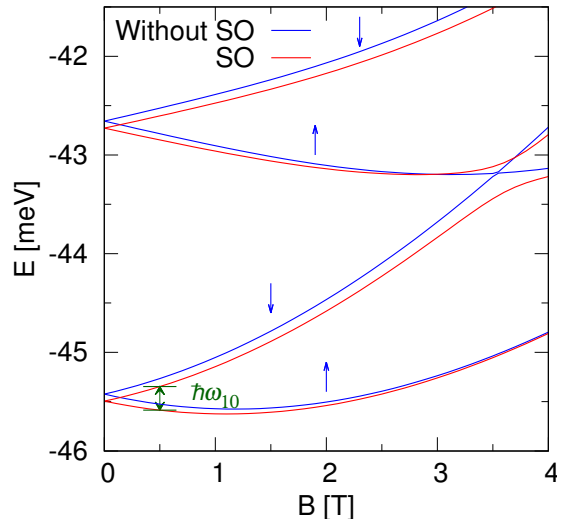


FIG. 3. The lowest single-electron energy levels as functions of the magnetic field for the rectangular elongated quantum dot ($V_b = 0$). Blue (red) lines show the levels obtained without (with) spin-orbit coupling. Blue arrows indicate the spin directions for corresponding energy levels without SO coupling. Green arrows mark the resonant frequency in the case of SO coupling for $B = 0.5$ T, $\omega_{10} = \frac{E_1 - E_0}{\hbar}$.

The ground-state and the first excited state at $B = 0$ remain two-fold degenerate in presence of the SO coupling. The states of the Kramers doublets correspond to opposite eigenvalues of $P\sigma_z$ operator⁴³, where P stands for the parity operator $Pf(r) = f(-r)$. The components of the wave functions are given in Fig. 4. The majority and minority spin components possess opposite symmetries with respect to point inversion across the origin.

We now consider the spin-flip or the transition between the ground state energy level and the first-excited energy level separated by $\hbar\omega_{10}$ [see Fig. 3]. For the initial condition of the spin-flip process we set the system in the ground-state, then we turn on the AC perturbation by the tip as given by Eq. (10). The maximal occupation of the spin-down state as calculated by the exact solution of the Schrödinger equation is plotted in Fig. 5(a) for varied tip locations and the AC pulse of 300 ps. For the tip at the center of the QD potential no spin transitions are observed (green line). When the tip is moved slightly off the origin (blue line) the transition becomes visible. For the tip off the symmetry axis of the QD potential (red line) the transition occurs much faster. The inset to Fig. 5(a) shows the results for the duration of

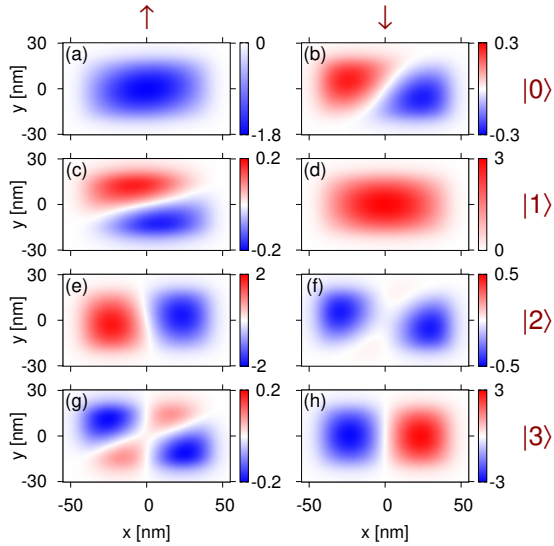


FIG. 4. Spin up (left column) and spin down (right column) components of single-electron wave functions for $B = 0.5$ T. The color scales give the real part of wave functions in units of $[10^{-2} \text{ nm}^{-1}]$. The ground state is denoted as $|0\rangle \equiv |\psi_0\rangle$ (cf. first row of plots), first excited state as $|1\rangle$, etc.

the AC signal increased to 250 ns. The transition probability reaches 1 for the tip off the origin, only the width of the transitions depends on the tip position. Besides the first order transition near $\hbar\omega = \hbar\omega_{10}$ the fractional resonances corresponding to multiphoton transitions are seen at lower energy side.

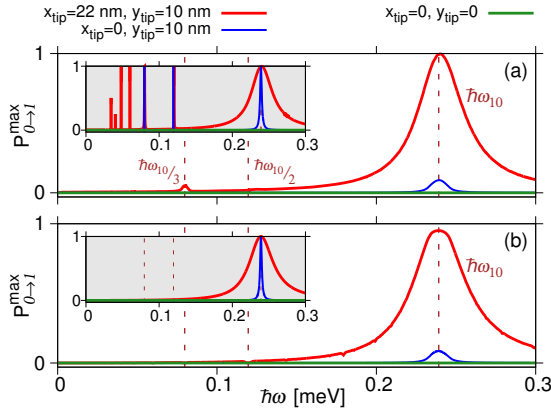


FIG. 5. Maximal probability of finding the electron in $|1\rangle$ state as a function of the AC frequency for three positions of the tip that are defined in a color legend. Vertical dashed lines indicate a few resonant frequencies: $\hbar\omega_{10}$, $\hbar\omega_{10}/2$, ... (a) Results of the solution of the time-dependent Schrödinger equation for a single electron. (b) Results obtained with the time-dependent perturbation theory of the first order. The simulations with the initial state $|\psi_i\rangle = |0\rangle$ lasted 300 ps (250 ns for the insets).

The transition probability as a function of the tip po-

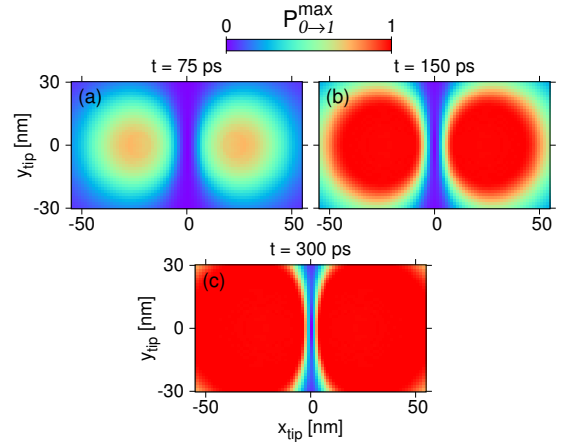


FIG. 6. Maximal occupation of the first excited state $|1\rangle$ for simulation lasting (a) 75 ps, (b) 150 ps, (c) 300 ps as function of the tip position. The frequency $\hbar\omega = 0.2392$ meV used in the calculations corresponds to the direct resonance (see Fig. 5(a)).

sition for $\hbar\omega = \hbar\omega_{10}$ is displayed in Fig. 6. In order to understand the dependence we use the first order perturbation theory, which correctly reproduces the direct spin-flipping transition – see Fig. 5(b). The transition to the excited state according to the first order perturbation [Eq. (17)] depends on the matrix element $\langle 1|V_T|0\rangle$ which is plotted in Fig. 7(a). The transition matrix element is strictly zero for $x_{\text{tip}} = y_{\text{tip}} = 0$ since the integrands for the spin-up and spin-down components [Fig. 4(a-d)] are of opposite parity. For that reason the transition matrix element for the tip at the symmetry center of the system vanishes. The matrix element possesses maxima off the $x_{\text{tip}} = 0$ axis of the plot [Fig. 7(a)] in consistency with the results of the time-dependent simulation [Fig. 6(a-c)]. Concluding, the spin-flip probability maps as functions of the tip position extract the form of the matrix elements with the integrands corresponding to the convolution of the minority/majority spin components of the wave functions with the potential of the tip. For the latter in the delta-like limit the matrix element tends to the overlap of the minority/majority spin components of the wave function. The form of the integrand of the matrix element for the adopted tip width of $d_{\text{tip}} = 20$ nm is displayed in Fig. 7(b).

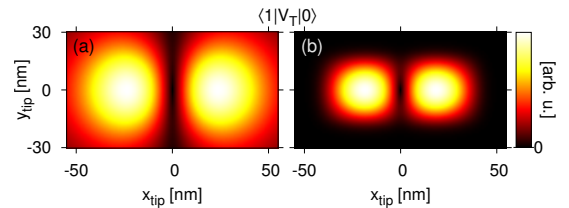


FIG. 7. (a) The absolute value of $\langle 1|V_T|0\rangle$ matrix element; panel (b) shows its integrand for $x = x_{\text{tip}}, y = y_{\text{tip}}$.

B. Double quantum dot

The energy spectrum for the two-electron system in the double quantum dot is displayed in Fig. 8. We consider the magnetic field of 1.2 T with the system in the T_+ ground state in which the flow of the current across the two quantum dots is blocked by Pauli exclusion, the hopping of the electron pair into one of the dots is forbidden by the fact that their spins are parallel. We focus on transitions to both states with zero component of the total spin in the z direction of the applied magnetic field, T_0 and S . In presence of the hyperfine coupling to the nuclear spin field these two states are actually mixed³⁴, in both the Pauli blockade is lifted²⁹ and the experimental EDSR spectra resolve both these lines.

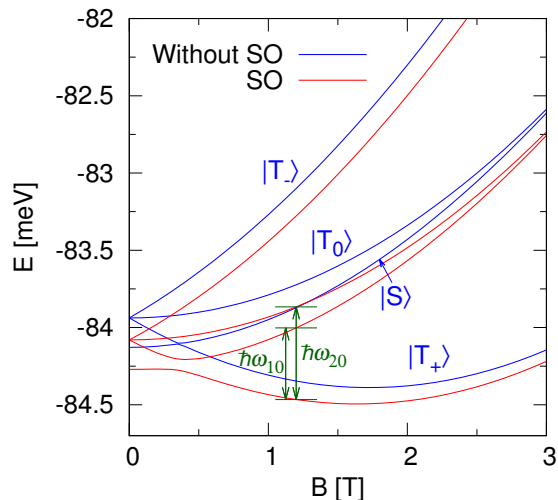


FIG. 8. The lowest two-electron energy levels as function of the magnetic field for two tunnel-coupled quantum dots ($V_b = 10$ meV). Blue (red) lines show the levels obtained without (with) spin-orbit coupling. Blue labels $|S\rangle$ and $|T_+\rangle$, $|T_0\rangle$, $|T_-\rangle$ indicate the energy levels of a singlet and the triplet states without SO coupling. Green arrows mark the resonant frequencies in the case of SO coupling for $B = 1.2$ T: $\omega_{10} = \frac{E_1 - E_0}{\hbar}$ and $\omega_{20} = \frac{E_2 - E_0}{\hbar}$; E_0 , E_1 and E_2 stand for the energies of $|T_+\rangle$, $|S\rangle$ and $|T_0\rangle$ states, respectively.

In Fig. 9(a) and (b) we present the transition probabilities to the S and T_0 states, respectively. The dependence of the transition rate on the tip position is found as in the single-electron case and for the transition to T_0 state the transition is absent for the tip at the center of the system. The transition maps as functions of the tip position are given in Figs. 10 and 11 for S and T_0 in the final state, respectively. The maps differ for the tip above the central part of the system, where a maximum (for S in Fig. 10) or a minimum (for T_0 in Fig. 11) is observed. Local maxima for the tip above the ends of the quantum dots are observed for both the final states, although for T_0 these maxima are more pronounced.

The corresponding matrix elements for the direct transitions are given in Fig. 12(a,b). The general positions

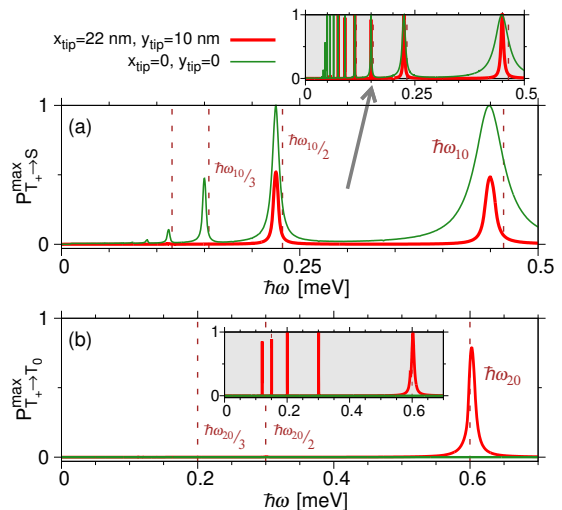


FIG. 9. Results of the solution of the time-dependent Schrödinger equation for the electron pair; $B = 1.2$ T is assumed. The simulations with the initial state $|\Psi_i\rangle = |T_+\rangle$ lasted 300 ps (250 ns for the insets). Maximal probabilities of finding the electron in $|S\rangle$ (upper panel) and $|T_0\rangle$ (lower panel) states as functions of the AC frequency for two positions of the tip that are defined in a color legend. Vertical dashed lines indicate a few resonant frequencies: $\hbar\omega_{10}$, $\hbar\omega_{10}/2$, \dots , and $\hbar\omega_{20}$, $\hbar\omega_{20}/2$, \dots

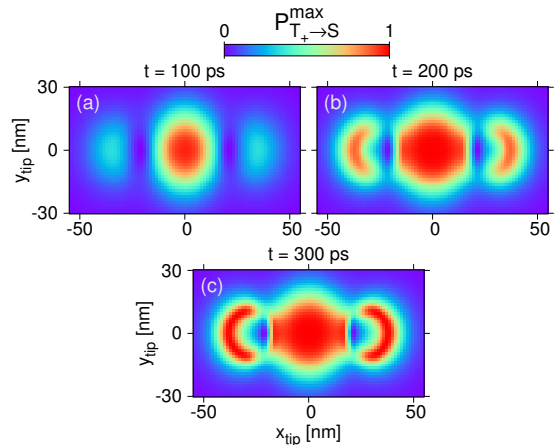


FIG. 10. Maximal occupation of the singlet state $|S\rangle$ for simulation lasting (a) 100 ps, (b) 200 ps, (c) 300 ps as function of the tip position. The frequency $\hbar\omega = 0.4486$ meV used in the calculations corresponds to the direct resonance (see Fig. 9(a)).

of the local extrema of the transition probability [Figs. 10 and 11] agree with the map of the matrix elements [Fig. 12(a,b)]. The characteristic arc-shaped features of Fig. 10(c) result from the Bloch-Siegert shifts⁴⁴⁻⁴⁶ of the resonant frequency (cf. the dashed line in Fig. 9(a) and the actual position of the direct resonance peak) which vary with the tip position. The maps in Figs. 10 and 11

are taken for fixed AC voltage frequency.

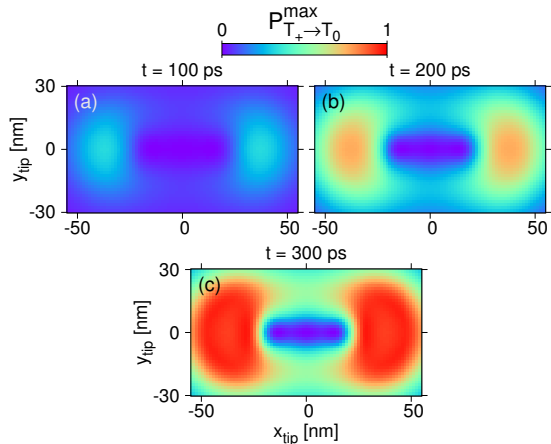


FIG. 11. Maximal occupation of the triplet state $|T_0\rangle$ for simulation lasting (a) 100 ps, (b) 200 ps, (c) 300 ps as function of the tip position. The frequency $\hbar\omega = 0.602$ meV used in the calculations corresponds to the direct resonance (see Fig. 9(b)).

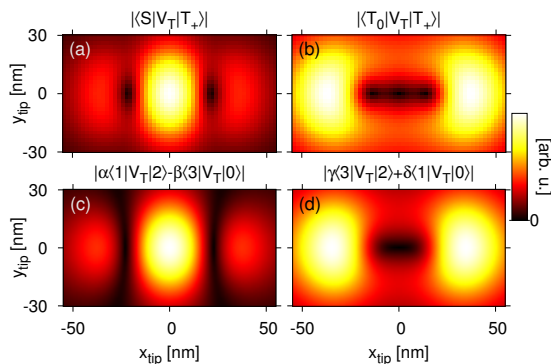


FIG. 12. The absolute values of (a) $\langle S|V_T|T_+\rangle$ and (b) $\langle T_0|V_T|T_+\rangle$ matrix elements as functions of the tip position. (c), (d) The corresponding approximations of $|\langle S|V_T|T_+\rangle|$ and $|\langle T_0|V_T|T_+\rangle|$ obtained with the formulas (18), (19).

In order to explain the form of the maps one has to analyze the contributions of the single-electron wave functions to the two-electron states. Figure 13 presents the spin-up and spin-down components of the single-electron states for the double quantum dot. The wave functions are still eigenstates of $P\sigma_z$ operator, with eigenvalues 1 for the ground state $|0\rangle$ and the third excited state $|3\rangle$ and -1 for the first and the second excited states ($|1\rangle$ and $|2\rangle$).

In Table I we listed the contributions of the Slater determinants to the two-electron states S, T_+ and T_0 . The two-electron states are eigenstates of the $P(1)\sigma_z(1)P(2)\sigma_z(2)$ with eigenvalues -1 for S and T_+ and $+1$ for T_0 . For the tip located at the center of the

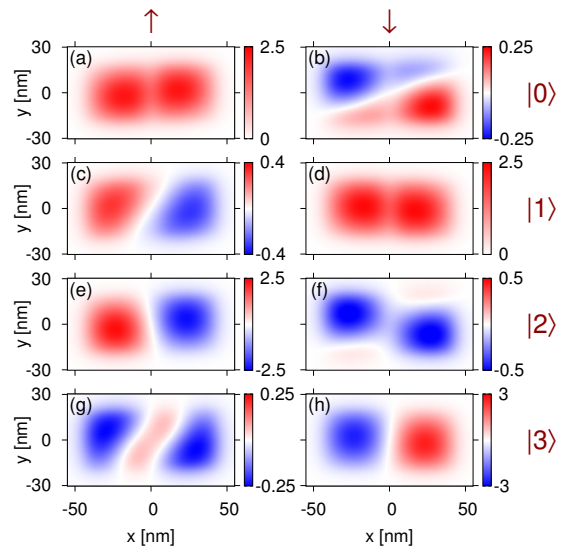


FIG. 13. Spin up (left column) and spin down (right column) components of the single-electron wave functions for $B = 1.2$ T in double quantum dot. The color scales give the real part of wave functions in units of $[10^{-2} \text{ nm}^{-1}]$. The ground state is denoted as $|0\rangle$ (cf. first row of the plots), first excited state as $|1\rangle$, etc.

system, the symmetry of the potential is unaffected and the transition matrix element $\langle T_0|V_T|T_+\rangle$ vanishes for the symmetry reasons. Only for the tip moved off the center the transition can be induced by the AC voltage applied to the tip. This explains the minimum of the transition maps from T_+ to T_0 in the center of the map [Fig. 11]. On the contrary, the transition from T_+ to S is allowed for the central position of the tip.

	$ T_+\rangle$
$\frac{1}{\sqrt{2}}(02\rangle - 20\rangle)$	0.8806
Other Slater determinants	0.1194
	$ S\rangle$
$\frac{1}{\sqrt{2}}(01\rangle - 10\rangle)$	0.5658
$\frac{1}{\sqrt{2}}(23\rangle - 32\rangle)$	0.2792
Other Slater determinants	0.1550
	$ T_0\rangle$
$\frac{1}{\sqrt{2}}(03\rangle - 30\rangle)$	0.4925
$\frac{1}{\sqrt{2}}(12\rangle - 21\rangle)$	0.4940
Other Slater determinants	0.0135

TABLE I. Slater determinants forming the basis and their contributions to $|T_+\rangle$, $|S\rangle$ and $|T_0\rangle$ states. The values are found by solving the eigenproblem of two-electron Hamiltonian for a double dot; $B = 1.2$ T.

For the two-electron wave functions reduced to the

principal contributions listed in Table I the form of the matrix elements can be expressed in terms of the single-electron matrix elements

$$\langle S|V_T|T_+\rangle \approx \alpha\langle 1|V_T|2\rangle - \beta\langle 3|V_T|0\rangle, \quad (18)$$

and

$$\langle T_0|V_T|T_+\rangle \approx \gamma\langle 3|V_T|2\rangle - \delta\langle 1|V_T|0\rangle, \quad (19)$$

where α , β , γ and δ are determined by the diagonalization of the two-electron Hamiltonian matrix in the Slater determinants basis. The form of the matrix elements for the approximated two-electron wave functions is given in Fig. 12(c,d) with a good agreement with the exact maps of Fig. 12(a,b).

IV. SUMMARY AND CONCLUSIONS

We have considered resonant spin transitions driven by the AC potential applied to tip of a scanning probe for a quantum dot in a semiconductor with spin-orbit coupling. The single-electron states were determined using a mesh of Gaussian functions and the two-electron

states were determined by the configuration-interaction method. The stationary Hamiltonian eigenstates were used for solution of the system dynamics with AC perturbation introduced by the probe. We demonstrated that the spin-transition rate strongly depends on the tip position and that the transition maps correspond closely to transition matrix elements with the tip potential. The latter involve the overlaps of the minority and majority spin components of the wave functions for the initial and final states with the tip potential. This opens an opportunity of experimental probing of the spatial distribution of the spin components for the confined wave functions. An experiment for the two-electron states in double quantum dot should resolve separate maps for the $T_+ \rightarrow S$ and $T_+ \rightarrow T_0$ transitions lifting the Pauli blockade of the current flow. The maps bear signatures of the two-electron spin-orbital symmetries and can be used for identification of the separate transition lines.

ACKNOWLEDGEMENTS

This work was supported by the National Science Centre according to decision DEC-2015/17/N/ST3/02282 and by PL-Grid Infrastructure.

-
- ¹ M. A. Topinka, B. J. LeRoy, S. E. J. Shaw, E. J. Heller, R. M. Westervelt, K. D. Maranowski, and A. C. Gossard, *Science* **289**, 2323 (2000).
- ² R. Crook, C. G. Smith, M. Y. Simmons, and D. A. Ritchie, *Phys. Rev. B* **62**, 5174 (2000).
- ³ A. Pioda, S. Kićin, T. Ihn, M. Sigrist, A. Fuhrer, K. Ensslin, A. Weichselbaum, S. E. Ulloa, M. Reinwald, and W. Wegscheider, *Phys. Rev. Lett.* **93**, 216801 (2004).
- ⁴ P. Fallahi, A. C. Bleszynski, R. M. Westervelt, J. Huang, J. D. Walls, E. J. Heller, M. Hanson, and A. C. Gossard, *Nano Lett.* **5**, 223 (2005).
- ⁵ K. E. Aidala, R. E. Parrott, T. Kramer, E. J. Heller, R. M. Westervelt, M. P. Hanson, and A. C. Gossard, *Nat. Phys.* **3**, 464 (2007).
- ⁶ A. A. Kozikov, D. Weinmann, C. Rössler, T. Ihn, K. Ensslin, C. Reichl, and W. Wegscheider, *New J. Phys.* **15**, 083005 (2013).
- ⁷ N. Pascher, F. Timpu, C. Rössler, T. Ihn, K. Ensslin, C. Reichl, and W. Wegscheider, *Phys. Rev. B* **89**, 245408 (2014).
- ⁸ M. Huefner, B. Kueng, S. Schnez, K. Ensslin, T. Ihn, M. Reinwald, and W. Wegscheider, *Phys. Rev. B* **83**, 235326 (2011).
- ⁹ K. Kolasinski, B. Szafran, B. Brun, and H. Sellier, *Phys. Rev. B* **94**, 075301 (2016).
- ¹⁰ A. C. Bleszynski-Jayich, L. E. Fröberg, M. T. Björk, H. J. Trodahl, L. Samuelson, and R. M. Westervelt, *Phys. Rev. B* **77**, 245327 (2008).
- ¹¹ E. E. Boyd, K. Storm, L. Samuelson, and R. M. Westervelt, *Nanotechnology* **22**, 185201 (2011).
- ¹² M. T. Woodside and P. L. McEuen, *Science* **296**, 1098 (2002).
- ¹³ X. Zhou, J. Hedberg, Y. Miyahara, P. Grutter, and K. Ishibashi, *Nanotechnology*, **25**, 495703 (2014).
- ¹⁴ J. Xue, R. Dhall, S. B. Cronin, and B. J. LeRoy, arXiv:1508.05462 (2015).
- ¹⁵ M. R. Connolly, K. L. Chiu, A. Lombardo, A. Fasoli, A. C. Ferrari, D. Anderson, G. A. C. Jones, and C. G. Smith, *Phys. Rev. B* **83**, 115441 (2011).
- ¹⁶ S. Morikawa, Z. Dou, S.-W. Wang, C. G. Smith, K. Watanabe, T. Taniguchi, S. Masubuchi, T. Machida, and M. R. Connolly, *Appl. Phys. Lett.* **107**, 243102 (2015).
- ¹⁷ S. Bhandari, G.-H. Lee, A. Klaes, K. Watanabe, T. Taniguchi, E. Heller, P. Kim, and R. M. Westervelt, *Nano Lett.* **16**, 1690 (2016).
- ¹⁸ H. Sellier, B. Hackens, M. G. Pala, F. Martins, S. Baltazar, X. Wallart, L. Desplanque, V. Bayot, and S. Huant, *Semicond. Sci. Technol.* **26**, 064008 (2011).
- ¹⁹ D. K. Ferry, A. M. Burke, R. Akis, R. Brunner, T. E. Day, R. Meisels, F. Kuchar, J. P. Bird, and B. R. Bennett, *Semicond. Sci. Technol.* **26**, 043001 (2011).
- ²⁰ W. G. van der Wiel, S. De Franceschi, J. M. Elzerman, T. Fujisawa, S. Tarucha, and L. P. Kouwenhoven, *Rev. Mod. Phys.* **75**, 1 (2002).
- ²¹ J. Qian, B. I. Halperin, and E. J. Heller, *Phys. Rev. B* **81**, 125323 (2010).
- ²² E. E. Boyd and R. M. Westervelt, *Phys. Rev. B* **84**, 205308 (2011).
- ²³ E. Wach, D. P. Żebrowski, and B. Szafran, *J. Phys.: Condens. Matter* **25**, 335801 (2013).
- ²⁴ E. Wach, D. P. Żebrowski, and B. Szafran, *Semicond. Sci. Technol.* **30**, 015020 (2015).
- ²⁵ F. H. L. Koppens, J. A. Folk, J. M. Elzerman, R. Hanson, L. H. Willems van Beveren, I. T. Vink, H. P. Tranitz, W.

- Wegscheider, L. P. Kouwenhoven, and L. M. K. Vandersypen, *Science* **309**, 1346 (2005).
- ²⁶ A. C. Johnson, J. R. Petta, C. M. Marcus, M. P. Hanson, and A. C. Gossard, *Phys. Rev. B* **72**, 165308 (2005).
- ²⁷ J. Stehlik, M. D. Schroer, M. Z. Maialle, M. H. Degani, and J. R. Petta, *Phys. Rev. Lett.* **112**, 227601 (2014).
- ²⁸ M. D. Schroer, K. D. Petersson, M. Jung, and J. R. Petta, *Phys. Rev. Lett.* **107**, 176811 (2011).
- ²⁹ S. Nadj-Perge, V. S. Pribiag, J. W. G. van den Berg, K. Zuo, S. R. Plissard, E. P. A. M. Bakkers, S. M. Frolov, and L. P. Kouwenhoven, *Phys. Rev. Lett.* **108**, 166801 (2012).
- ³⁰ E. A. Laird, C. Barthel, E. I. Rashba, C. M. Marcus, M. P. Hanson, and A. C. Gossard, *Phys. Rev. Lett.* **99**, 246601 (2007); E. A. Laird, C. Barthel, E. I. Rashba, C. M. Marcus, M. P. Hanson, and A. C. Gossard, *Semicond. Sci. Tech.* **24** 064004 (2009).
- ³¹ F. H. L. Koppens, C. Buizert, K. J. Tielrooij, I. T. Vink, K. C. Nowack, T. Meunier, L. P. Kouwenhoven, and L. M. K. Vandersypen, *Nature* **442**, 766 (2006).
- ³² E. I. Rashba and A. L. Efros, *Phys. Rev. Lett.* **91**, 126405 (2003); V. N. Golovach, M. Borhani, and D. Loss, *Phys. Rev. B* **74**, 165319 (2006).
- ³³ F. Forster, M. Mühlbacher, D. Schuh, W. Wegscheider, and S. Ludwig, *Phys. Rev. B* **91**, 195417 (2015).
- ³⁴ F.H.L. Koppens, J.A. Folk, J.M. Elzerman, R. Hanson, L.H. Wilems van Beveren, I.T. Vink, H.P. Tranitz, W. Wegscheider, L.P. Kouwenhoven, and L.M.K. Vandersypen, *Science* **309**, 1346 (2005).
- ³⁵ G. Dresselhaus, *Phys. Rev.* **100**, 580 (1955).
- ³⁶ C. F. Destefani, S. E. Ulloa, and G. E. Marques, *Phys. Rev. B* **70**, 205315 (2004).
- ³⁷ S. Saikin, M. Shen, M.-C. Cheng, and V. Privman, *J. Appl. Phys.* **94**, 1769 (2003).
- ³⁸ I. Vurgaftman, J. R. Meyer, and L. R. Ram-Mohan, *J. Appl. Phys.* **89**, 5815 (2001).
- ³⁹ M. Willatzen and L. C. Lew Yan Voon, *J. Phys.: Condens. Matter* **20**, 345216 (2008).
- ⁴⁰ R. Winkler, *Spin-Orbit Coupling Effects in Two-Dimensional Electron and Hole Systems*, Springer Tracts in Modern Physics Vol. 191 (Springer, Berlin 2003).
- ⁴¹ B. Szafran, *Phys. Rev. B* **84**, 075336 (2011).
- ⁴² A. Askar and A. S. Cakmak, *J. Chem. Phys.* **68**, 2794 (1978).
- ⁴³ E. N. Osika, B. Szafran, and M. P. Nowak, *Phys. Rev. B* **88**, 165302 (2013).
- ⁴⁴ J. H. Shirley, *Phys. Rev.* **138**, B979 (1965).
- ⁴⁵ F. Bloch and A. Siegert, *Phys. Rev.* **57**, 522 (1940).
- ⁴⁶ J. Romhányi, G. Burkard, and A. Pályi, *Phys. Rev. B* **92**, 054422 (2015).